

Daytime Local Circulations and Their Interactions in the Seoul Metropolitan Area

YOUNG-HEE RYU AND JONG-JIN BAIK

School of Earth and Environmental Sciences, Seoul National University, Seoul, South Korea

(Manuscript received 21 June 2012, in final form 11 November 2012)

ABSTRACT

Daytime local circulations and their interactions in the Seoul, South Korea, metropolitan area are investigated using a high-resolution mesoscale model. It is found that the urban-breeze circulation interacts strongly with other local circulations, such as sea-breeze, cross-valley, and river-breeze circulations. Inland penetration of the sea breeze is retarded in the morning when moving over the coastal urban area because of the increased surface roughness but is accelerated in the afternoon after passing through the urban area as a result of the landward-convergent flow induced by urban heat islands in the inland urban areas. In the valley region, the cross-valley circulation prevails in the morning and the urban-breeze circulation prevails in the afternoon. The mountainside urban-breeze circulation weakens because of the cross-valley circulation in the opposite direction. On the other hand, the plainside urban-breeze circulation away from the mountain increases in strength as a result of the combined effect of heating from the urban surface and subsidence heating associated with the cross-valley circulation. This strengthened urban breeze acts to inhibit penetration of the sea breeze farther inland, causing the sea breeze to stagnate in Seoul. In the vicinity of the Han River, convergence zones with strong updrafts are formed as a result of the interaction between the urban breeze and the river breeze. When the sea-breeze front encounters the strong updrafts, the vertical velocity of the front at the intersection points increases.

1. Introduction

The higher air temperature in a city than in its surrounding rural area, which is known as the urban heat island (UHI), can generate or modify local circulations in the city and its vicinity. When the synoptic forcing is weak, a local circulation can develop in regions where a temperature contrast exists, such as between sea and land, lake and land, river and land, and mountain and valley. Besides well-known local circulations such as sea-breeze and valley-breeze circulations, a local circulation due to the presence of a city has been observed in many cities: for example, St. Louis, Missouri (Wong and Dirks 1978), and Toulouse, France (Hidalgo et al. 2008b). In the daytime, a local circulation that is characterized by inward flow toward a city center in the lower boundary layer and outward flow toward the surrounding rural area in the upper boundary layer is induced by the temperature contrast between the city and its surrounding rural

area (i.e., UHI). This circulation is called the urban-breeze circulation or the UHI circulation. Urban-breeze circulations have been investigated numerically and found to have maximum intensities in the late afternoon, with horizontal velocities of $2\text{--}7 \text{ m s}^{-1}$ and vertical velocities of $\sim 1 \text{ m s}^{-1}$ (e.g., Lemonsu and Masson 2002; Hidalgo et al. 2008a).

Many studies of urban impacts on sea breeze have been undertaken. It has been reported that the inland penetration of sea breeze is retarded because of the increased surface roughness of cities, particularly in coastal cities such as New York City, New York (e.g., Bornstein and Thompson 1981; Thompson et al. 2007); Athens, Greece (Dandou et al. 2009); and Houston, Texas (Chen et al. 2011). For inland cities such as Brisbane, Australia (Khan and Simpson 2001), and Sao Paulo, Brazil (Freitas et al. 2007), it has been shown that the inland penetration of sea breeze is accelerated owing to the landward-convergent flow induced by the UHI. After the arrival of sea breeze in a city, the inward flow toward the city center that forms part of the urban breeze acts to inhibit penetration of the sea breeze farther inland (e.g., Yoshikado 1992; Freitas et al. 2007). In particular, for an inland city located sufficiently far from the coast, an

Corresponding author address: Jong-Jin Baik, School of Earth and Environmental Sciences, Seoul National University, Seoul 151-742, South Korea.
E-mail: jjbaik@snu.ac.kr

urban breeze has ample time to develop and hence can have a considerable impact on a sea breeze, as emphasized by Yoshikado (1994) and Freitas et al. (2007).

Many cities in the world are located in valley regions, and therefore local circulations induced by urban/rural land-use contrast and by mountain-valley topography can interact with each other. By conducting two-dimensional idealized numerical experiments, Lee and Kimura (2001) examined the evolutions of local circulations induced by land-use contrast (bare soil and vegetation) and by topography and the relative importance of the local circulations. Note that the local circulation induced by the large temperature contrast between bare soil and vegetation can be regarded as being similar to that between a city and its surrounding rural area, particularly in the daytime. They found that in the morning cross-valley circulation prevails in the whole area and the circulation induced by the land-use contrast does not appear. As the circulation induced by the land-use contrast increases in strength in the afternoon, it predominates over the cross-valley circulation. Because the two circulations are opposite in direction, the cross-valley circulation weakens in the afternoon. By conducting two-dimensional idealized numerical experiments, Ohashi and Kida (2002) showed that urban-breeze circulation weakens owing to cross-valley circulation.

There have been a few studies addressing urban impacts on river breeze. For example, Shreffler (1978) documented that the inward flow toward the warm core of St. Louis is stronger at the station adjacent to the Mississippi River than at other stations and hypothesized that the stronger inflow may reflect a component of the river breeze.

As demonstrated in the previous studies mentioned above, a city can induce local circulation and this circulation can modify or interact with other local circulations. The objective of this study is to examine daytime local circulations, such as urban-breeze, sea-breeze, cross-valley, and river-breeze circulations, and their interactions in the Seoul metropolitan area through a case study. A clear day in summer (24 June 2010) is chosen for this case study. The Seoul metropolitan area (SMA) is the largest urban area in South Korea and is characterized by complex geographical features. The SMA is adjacent to the Yellow Sea to the west, several mountains are located near Seoul, and the Han River passes through Seoul (Figs. 1b,c). Thus, several local circulations can develop in the SMA under favorable weather conditions and the local circulations can interact with each other. To resolve the detailed features of the local circulations and their interactions, high-resolution simulations are performed using a mesoscale atmospheric model. In addition, a state-of-the-art single-layer urban

canopy model is employed in this study to better represent and simulate the physical processes occurring in an urban canopy.

The description of the mesoscale atmospheric model that is coupled with the urban canopy model and the experimental design are given in section 2. In section 3, the meteorological condition for the case is described and the model is validated against observations. Results are presented and discussed in section 4. A summary and conclusions are given in section 5.

2. Model description and experimental design

The Advanced Research Weather Research and Forecasting (WRF) model, version 3.2 (Skamarock et al. 2008), is employed in this study. The Seoul National University Urban Canopy Model (SNUUCM; Ryu et al. 2011) is used as an urban module. The urban canopy model is a single-layer urban canopy model and parameterizes many important physical processes occurring in an urban canopy. In this study, two canyon orientations perpendicular to each other (north–south and east–west orientations) are considered as representative canyon orientations in the study area. The energy fluxes from the two canyons are then averaged. Table 1 lists the values of urban surface parameters used in this study. The SNUUCM is coupled with the Noah land surface model (LSM; Chen and Dudhia 2001) in a tile approach in the WRF model. In other words, energy fluxes for a built-up area in an urban area are calculated by using the SNUUCM, those for a natural area in an urban area are calculated by using the Noah LSM, and the output energy fluxes are then area weighted for urban-averaged energy fluxes.

Five computational domains with two-way interactions are considered (Fig. 1a). The horizontal grid spacings are 27, 9, 3, 1, and 0.333 km. The total number of vertical layers below a model top of 20 hPa is 43, and there are 16 vertical layers below 2 km. The vertical grid spacing is stretched with height, starting from ~ 35 m above the surface. To damp out poorly resolved kinematical features with wavelengths of 2–4 times the horizontal grid spacing, the sixth-order spatial filter developed by Knievel et al. (2007) is used. This filter acts to effectively damp out small-scale features. The model is integrated for 72 h, starting from 0000 UTC (=0830 LST) 22 June 2010. The time step for the outermost domain is 60 s, and the time steps for the inner domains are reduced by one-third of the time step for their outer domains. As the initial and boundary conditions, the National Centers for Environmental Prediction final analysis data with $1^\circ \times 1^\circ$ horizontal resolution in 6-h intervals are used. Physical parameterization options used are the Dudhia shortwave

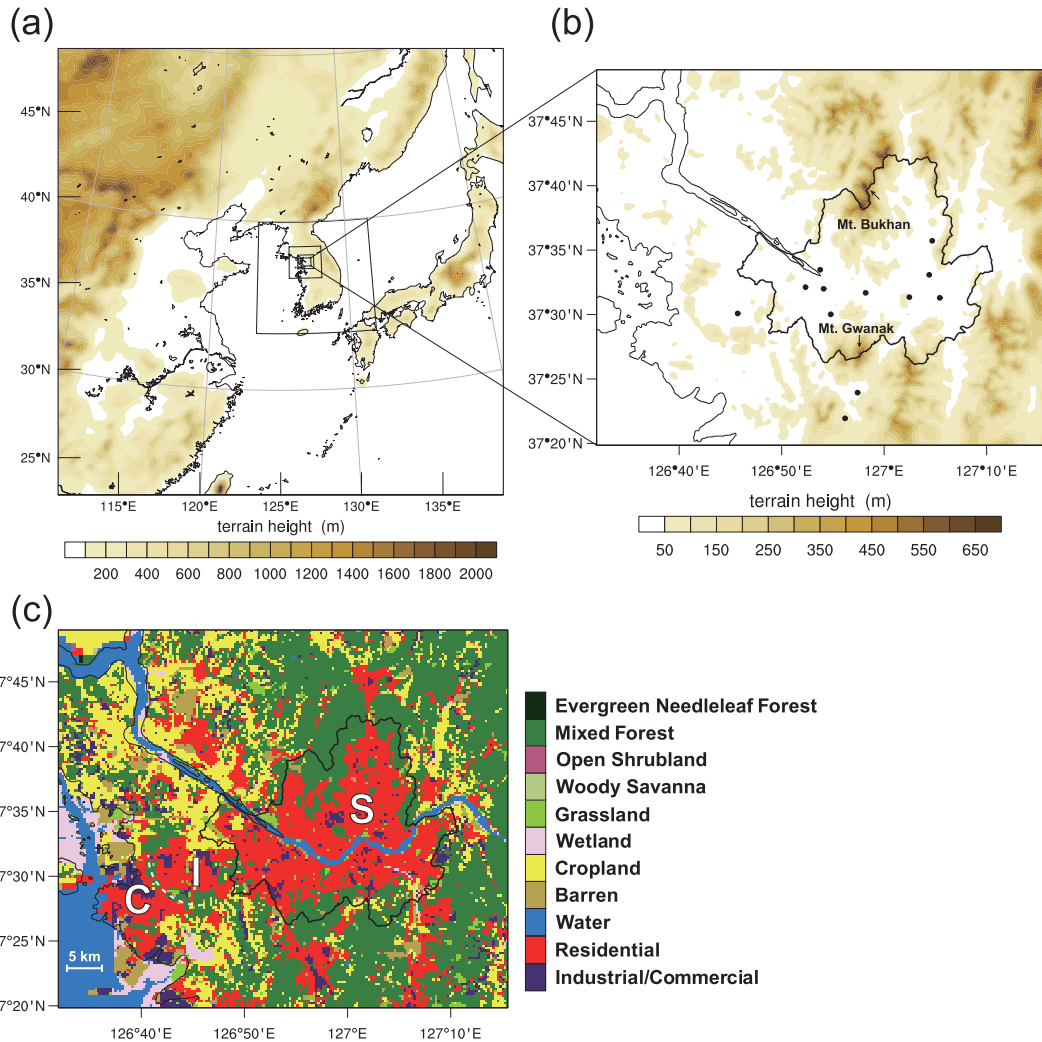


FIG. 1. (a) The five domains and (b) the innermost domain in the WRF-SNUUCM simulation with terrain height (shaded). (c) LULC in the innermost domain. Note that Mount Bukhan and Mount Gwanak are located at the northern and southern borders of Seoul, respectively, and their summits are indicated by arrows in (b). The 12 urban stations selected for the model validation are marked by dots in (b). The C, I, and S in (c) stand for coastal urban area, inland urban area, and Seoul urban area (farther-inland urban area), respectively. The boundary between the coastal and inland urban areas is indicated by the dashed line in (c). The administrative boundary of Seoul is marked by a thick black line in (b) and (c).

radiation scheme (Dudhia 1989), the Rapid Radiative Transfer Model (RRTM) longwave radiation scheme (Mlawer et al. 1997), the Noah LSM, the Yonsei University planetary boundary layer scheme (Hong et al. 2006), and the WRF single-moment 6-class microphysics scheme (Hong and Lim 2006). The updated Kain–Fritsch convective scheme (Kain 2004) is used as a cumulus parameterization scheme only for the domains with horizontal grid spacings of 27 and 9 km. The horizontal and vertical second spatial filtering on model coordinate surfaces is considered, and for the horizontal eddy viscosity the Smagorinsky first-order closure approach is

adopted. For the case selected for this study, horizontal vortices that can be formed in high-resolution numerical simulations for particular cases (e.g., Bornstein et al. 2012) do not appear with the experimental design described in this section.

The global topography data provided by the U.S. Geological Survey have a horizontal resolution of 30 s (~ 1 km), and hence they are not suitable as surface boundary data for a high-resolution simulation. The topography data ranging from 37° to 38° N and from 126° to 128° E are therefore updated based on the Shuttle Radar Topography Mission (SRTM) data (Farr et al.

TABLE 1. Values of urban surface parameters and anthropogenic heat intensity used in the WRF-SNUUCM simulation. The anthropogenic heat intensity is based on the work of Lee et al. (2009). The roughness lengths for momentum and heat are denoted by $z_{0,m}$ and $z_{0,\theta}$, respectively.

Parameters	Industrial/commercial	Residential
Area fractions		
Built-up area	0.9	0.815
Natural area	0.1	0.185
Geometric parameters		
Mean building height (m)	15	10
Canyon aspect ratio	1.0	0.5
Roof fraction	0.6	0.6
Ratio $z_{0,m}/z_{0,\theta}$ for canyon air	10	10
Roof and wall properties		
Albedo	0.12	0.12
Emissivity	0.95	0.95
Heat capacity ($\text{MJ m}^{-3} \text{K}^{-1}$)	1.0	1.0
Thermal conductivity ($\text{W m}^{-1} \text{K}^{-1}$)	0.67	0.67
Ratio $z_{0,m}/z_{0,\theta}$ (only for roof)	10	10
Road properties		
Albedo	0.08	0.08
Emissivity	0.95	0.95
Heat capacity ($\text{MJ m}^{-3} \text{K}^{-1}$)	1.4	1.4
Thermal conductivity ($\text{W m}^{-1} \text{K}^{-1}$)	0.4	0.4
Ratio $z_{0,m}/z_{0,\theta}$	10	10
Anthropogenic heat intensity (W m^{-2})		
Max	43	27
Min	19	12
Avg	33	21

2007) that have a horizontal resolution of 3 s (~ 90 m), providing a good representation of the finescale topography in the SMA (Fig. 1b).

The accurate representation of land use/land cover (LULC) of an urban area is important in studying urban-related phenomena. Hence, a new LULC dataset based on geographic information system data (with a horizontal resolution of 4 m) established by the Korea Ministry of Environment in 2009 is utilized, which covers the SMA. The new LULC dataset originally has six urban categories: industrial, commercial, residential, recreational, transport, and public facility. In this study, the six urban categories are recategorized into two urban categories: industrial/commercial and residential. The industrial and commercial categories of the new LULC dataset are combined into the industrial/commercial category, and the remaining four categories are combined into the residential category. Different values of urban surface parameters and anthropogenic heat intensities are applied to the two categories (see Table 1). Note that to examine urban impacts an additional simulation (NO-URBAN simulation) is performed in which the urban area in the SMA is replaced with cropland. That is, in the NO-URBAN simulation, no urban grid is present

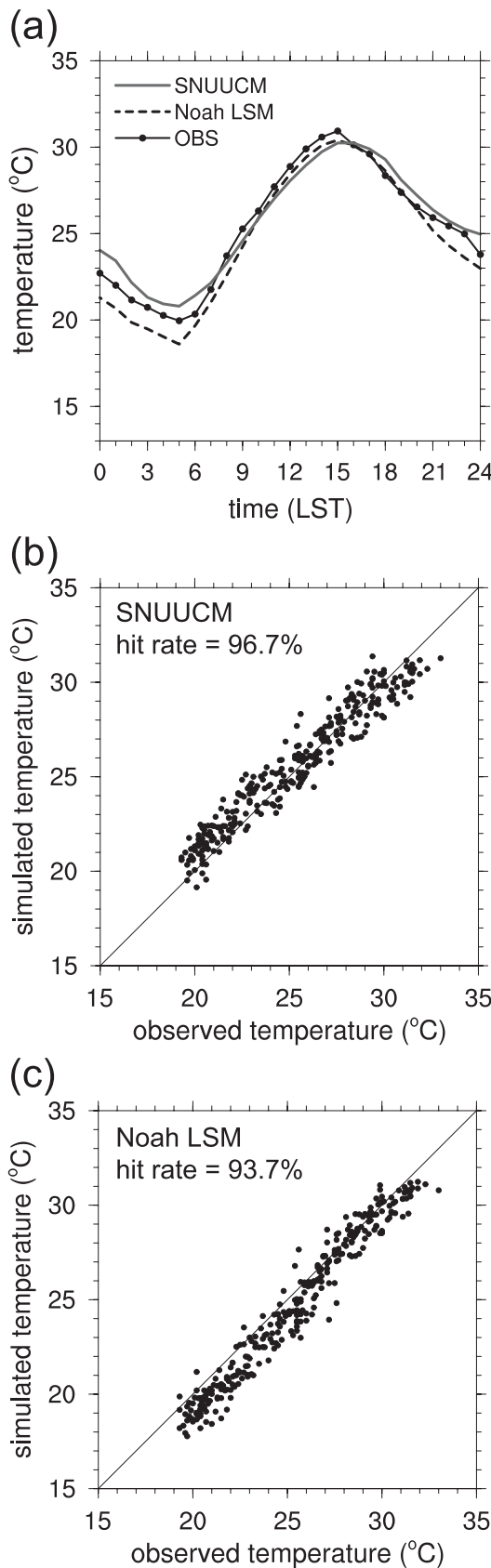
in the SMA so the Noah LSM is applied to the cropland grids in the SMA. For the LULC in the region outside the SMA, the Moderate Resolution Imaging Spectroradiometer (MODIS) LULC dataset is used.

The Han River passes through the SMA (Fig. 1c). In the WRF model, the surface temperature of water body is not a prognostic variable. Accordingly, the river surface temperature is held constant during the entire integration. To provide more realistic boundary conditions, the daytime-averaged river surface temperature observed at Guri station ($37.58^\circ\text{N}, 127.16^\circ\text{E}$) of 24.0°C is used.

3. Meteorological condition and model validation

A high pressure system prevailed over the Korean Peninsula on 23–24 June 2010. Under the influence of the high pressure system, low-level winds in the SMA remained weak. The daytime wind speed observed at 850-hPa level on 24 June 2010 was lower than 4 m s^{-1} . Thus, the meteorological condition on 24 June 2010 was favorable for the development of local circulations. In particular, the weak offshore (easterly) synoptic wind provides a favorable condition for the development of a sea-breeze circulation with a distinct and intense sea-breeze front, as pointed out by Crosman and Horel (2010). In this study area, similar meteorological conditions are often observed in warm/hot months.

The simulated near-surface air temperature is validated against the observed one at 12 urban stations in the SMA, and the performance of the SNUUCM is compared with that of the Noah LSM (Fig. 2). The 12 urban stations that belong to the automatic weather stations operated by the Korea Meteorological Administration are marked by dots in Fig. 1b. In the Noah LSM simulation, the Noah LSM is used solely as a slab model and the SNUUCM is not incorporated. Figure 2a shows that both models slightly underestimate the maximum temperature but well reproduce the diurnal variation of temperature. While the Noah LSM tends to underestimate both daytime and nighttime temperatures (Fig. 2c), the SNUUCM simulates higher nighttime temperatures than the Noah LSM does (Fig. 2b). The hit rate, which is defined as the percentage of simulated values within a desired accuracy range of the observed ones, is calculated for the simulations. The accuracy range for temperature is set as $\pm 2^\circ\text{C}$, following Ries and Schlünzen (2009). Judging by the hit rate, the SNUUCM (96.7%) performs better than the Noah LSM (93.7%). The simulated near-surface wind is compared with observed one, and the SNUUCM shows a satisfactory performance in reproducing the diurnal variation of observed wind speed and the intrusion of sea breeze (not shown).



4. Results and discussion

a. Local circulations in the SMA

Figure 3 shows the diurnal variations of sensible heat flux, latent heat flux, air temperature at 2 m, and boundary layer height averaged over all the urban grids in the URBAN simulation and the corresponding cropland grids in the NO-URBAN simulation. The boundary layer height under unstable conditions is determined to be the first neutral level using the bulk Richardson number (Hong et al. 2006; Shin and Hong 2011). In this study, urban impacts are examined by comparing the results of the URBAN simulation with those of the NO-URBAN simulation. Note that in this study simulation data in the innermost domain are used for all the analyses. It is well known that the sensible heat flux from urban areas is generally larger than that from surrounding rural areas owing to distinctive urban-surface characteristics, such as low surface moisture availability and large thermal inertia, and owing to the emission of anthropogenic heat. Figures 3a and 3b show the typical features of sensible and latent heat fluxes observed in many cities and their surroundings (e.g., Hidalgo et al. 2008b). As a result of the larger sensible heat flux from the urban area, the air temperature is higher and the boundary layer height is also higher in the URBAN simulation than in the NO-URBAN simulation. The UHI intensity, which is defined in this study as the difference in air temperature between the two simulations, is strong in the nighttime. The daytime UHI intensity is weak in the morning (e.g., 0.2°C at 1000 LST) and increases in the afternoon (e.g., 1.0°C at 1600 LST). These characteristics of the daytime UHI are consistent with those observed in many cities (e.g., Kim and Baik 2002; Giridharan et al. 2007; Hidalgo et al. 2008b). As reported in a number of observational and modeling studies, the urban boundary layer is deeper by several hundreds of meters than the rural boundary layer (e.g., Dirks 1974; Hidalgo et al. 2008a). For example, the difference in boundary layer height at 1600 LST between the two simulations is 379 m.

In the SMA, urban-breeze, cross-valley, river-breeze, and sea-breeze circulations develop under the weak synoptic-wind condition. To illustrate the local circulations, near-surface air temperature and wind fields in the URBAN and NO-URBAN simulations are presented in

←

FIG. 2. (a) Diurnal variations of near-surface air temperature observed at 12 urban stations and simulated by the SNUUCM and Noah LSM on 24 Jun 2010. Scatterplots of near-surface air temperature observed vs that simulated by the (b) SNUUCM and (c) Noah LSM.

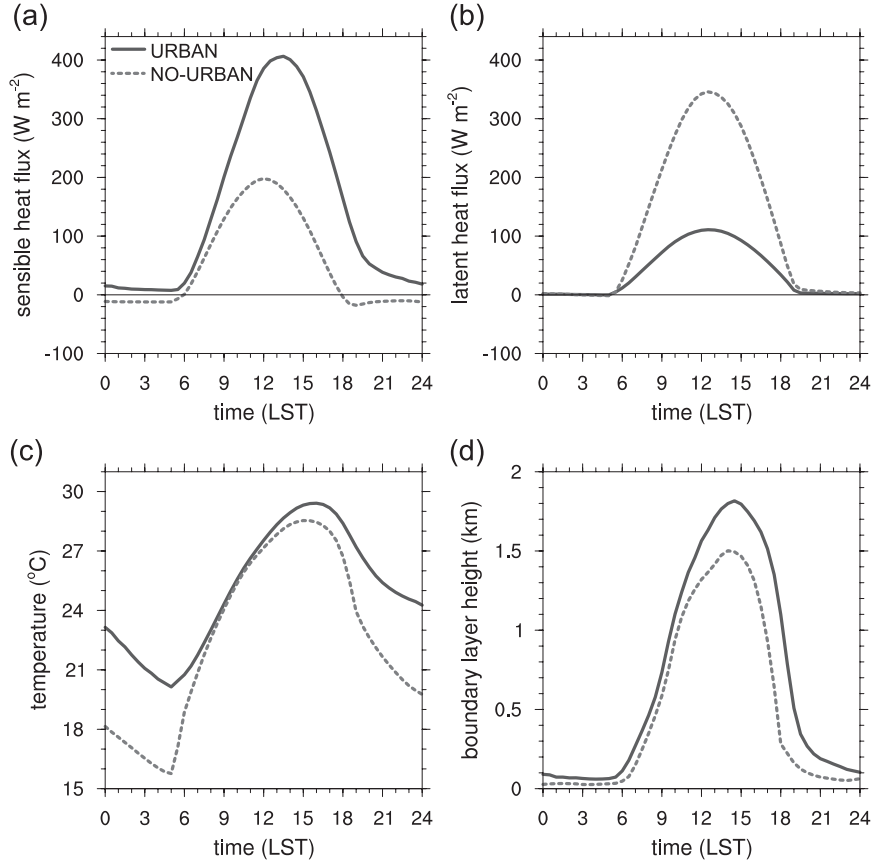


FIG. 3. Diurnal variations of (a) sensible heat flux, (b) latent heat flux, (c) air temperature at 2 m, and (d) boundary layer height averaged over all the urban grids in the URBAN simulation and the corresponding cropland grids in the NO-URBAN simulation.

Fig. 4. In both simulations, a sea breeze and a river breeze start to develop in the morning near the coastal area and near the Han River, respectively (Figs. 4a,b). The Han River divides Seoul into northern and southern areas. In this study, the northern (southern) area of Seoul refers to the area to the north (south) of the Han River. Upslope winds develop in the vicinity of mountains, such as Mount Bukhan and Mount Gwanak, in both simulations. The wind fields in the two simulations are rather similar to each other. This is because the difference in thermal forcing between the urban surface and cropland is small in the morning.

As the daytime UHI intensity increases in the afternoon (Fig. 3c), the wind fields in the two simulations exhibit different features (Figs. 4c,d). The air temperature over Seoul in the URBAN simulation is up to 1.6°C higher than that in the NO-URBAN simulation. The most remarkable feature in the URBAN simulation is the formation of a convergence zone associated with an urban-breeze circulation near the northeastern area of Seoul. In the northern area of Seoul adjacent to Mount

Bukhan, the upslope wind that develops in the morning is indiscernible. The interaction between the urban-breeze and cross-valley circulations is described in section 4b. On the other hand, in the NO-URBAN simulation, the upslope wind prevails in the vicinities of Mount Bukhan and Mount Gwanak. In addition, an along-valley circulation develops in the northern and southern areas of Seoul. In those areas, the along-valley circulation is combined with the river-breeze circulation, so a southerly (northerly) wind prevails in the northern (southern) area of Seoul.

Another convergence zone is formed in the southern area of Seoul adjacent to the Han River in the URBAN simulation (Fig. 4c). This is a result of the interaction between the urban breeze and the river breeze, and the detailed analysis results are given in section 4c.

In both simulations, the sea breeze that initially develops in the morning penetrates inland as time passes. The sea breeze is greatly influenced by Seoul and nearby cities. For example, in the presence of the urban area, the sea breeze penetrates farther inland (cf. Fig. 4c with Fig. 4d) and stalls near the eastern boundary of Seoul in

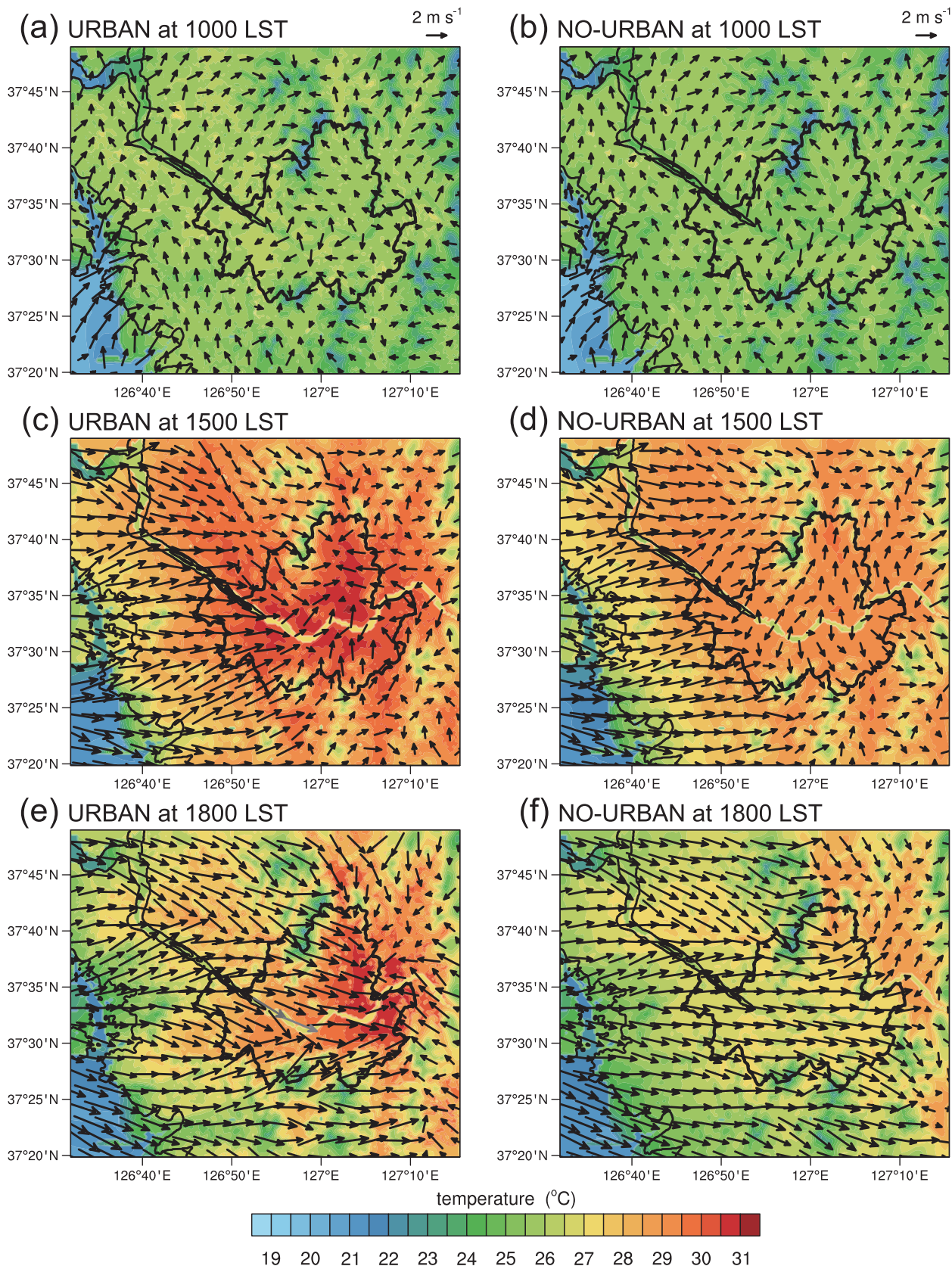


FIG. 4. Fields of air temperature at 2 m and wind (vectors) at 10 m at (a) 1000, (c) 1500, and (e) 1800 LST in the URBAN simulation and at (b) 1000, (d) 1500, and (f) 1800 LST in the NO-URBAN simulation.

the early evening (cf. Fig. 4e with Fig. 4f). The detailed analysis results are given in section 4d.

b. Cross-valley circulation and its interaction with urban-breeze circulation

To examine the evolutions of cross-valley and urban-breeze circulations and their interaction, the vertical cross sections of potential temperature anomaly and wind along the line A–B (depicted in Fig. 8a, described in more detail below) are presented in Fig. 5. The line A–B is chosen to show representative examples of the two circulations. Here, the potential temperature anomaly is calculated at each level by subtracting the average value from the total value. In the morning, the upslope wind is driven by the horizontal temperature contrast between the air near the mountain slope and the air at the same level over the plain. In both simulations, the upslope wind along the slope of Mount Bukhan and the associated cross-valley circulation are evident (Figs. 5a,b). The wind patterns in the two simulations are rather similar to each other, but the intensity of the cross-valley circulation at 1000 LST is weaker in the URBAN simulation than in the NO-URBAN simulation. This is because the higher air temperature in the urban valley acts to inhibit the development of a stronger cross-valley circulation.

At noon, the air temperature in the valley increases in the URBAN simulation. As a result, an inward flow toward the valley center starts to develop in the lower boundary layer (Fig. 5c). The leading edges of the urban-breeze circulation are detected by the two updrafts near points V1 and V2 in Fig. 5e (also see Fig. 8c, described below), and the two updrafts move toward the valley center. The updrafts finally merge with each other near the valley center at 1500 LST, which results in a strong upward motion (Fig. 5g). (The strong updraft and well-developed urban breeze are also evident in Fig. 8d, described in more detail below.) Because the air temperature in the urban valley is high, the cross-valley circulation whose direction is opposite to the direction of the mountainside urban-breeze circulation weakens and eventually becomes insignificant, unlike the cross-valley circulation in the NO-URBAN simulation. Thus, similar to the result of Lee and Kimura (2001), in the afternoon the urban-breeze circulation predominates over the cross-valley circulation.

The time variations of horizontal convergence averaged over the rectangular area (Fig. 8a, below) in the URBAN and NO-URBAN simulations are compared (Fig. 6). Here, the positive values (convergence) are averaged to take into account the urban-breeze and cross-valley circulations that can produce horizontal convergence at the low atmospheric level. The rectangular area (Fig. 8a, below) is chosen to exclude the effect of the sea breeze.

Note that the sea-breeze front arrives in this area at \sim 1610 LST. During 0900–1045 LST, the horizontal convergence in the NO-URBAN simulation is stronger than that in the URBAN simulation. The weaker horizontal convergence in the morning in the URBAN simulation means that the cross-valley circulation weakens owing to the presence of the urban area, as shown in Figs. 5a and 5b. However, the horizontal convergence in the URBAN simulation increases in the late morning/early afternoon and becomes much stronger in the late afternoon than that in the NO-URBAN simulation. The strong convergence in the urban valley results from the combined effect of heating from the urban surface and subsidence heating associated with the cross-valley circulation.

Figures 5c and 5e show that the air temperature near the mountain (near point V1) is higher than that near the valley center. In addition, the updraft near point V1 is stronger than that near point V2. The large temperature anomaly near point V1 is related to the adiabatic heating by the downward motion of the cross-valley circulation (subsidence heating). Figure 7 shows the time-height fields of the term of the vertical advection of potential temperature ($-w\partial\theta/\partial z$) in the thermodynamic energy equation at points V1 and V2 in the URBAN simulation. Here, w is the vertical velocity, θ is the potential temperature, and z is the vertical coordinate. Subsidence heating is evident in the morning near the top of the boundary layer, particularly prominent at point V1. This subsidence heating contributes to increasing the air temperature in the valley, as demonstrated by Rampanelli et al. (2004). Thus, this suggests that in the urbanized basin area not only the large sensible heat (resulting in the UHI) but also the subsidence heating plays an important role in increasing the air temperature. The stronger subsidence heating at point V1 than at point V2 implies that the stronger heating associated with the stronger cross-valley circulation is a responsible factor for the larger temperature anomaly.

It is shown that the direction of the mountainside urban-breeze circulation is opposite to that of the cross-valley circulation. It is interesting that the intensity of the plainside urban-breeze circulation (e.g., near point V2) is stronger than that of the mountainside urban-breeze circulation (e.g., near point V1) (Figs. 5c,e,g). As compared with the urban-breeze circulation in a simulation without topography, the intensity of the mountainside urban-breeze circulation in the URBAN simulation with topography is evidently weaker, but the intensity of the plainside urban-breeze circulation is stronger (not shown). The strengthened plainside urban-breeze circulation away from the mountain is because of the combined effect of heating from the urban surface and subsidence heating due to the cross-valley circulation.

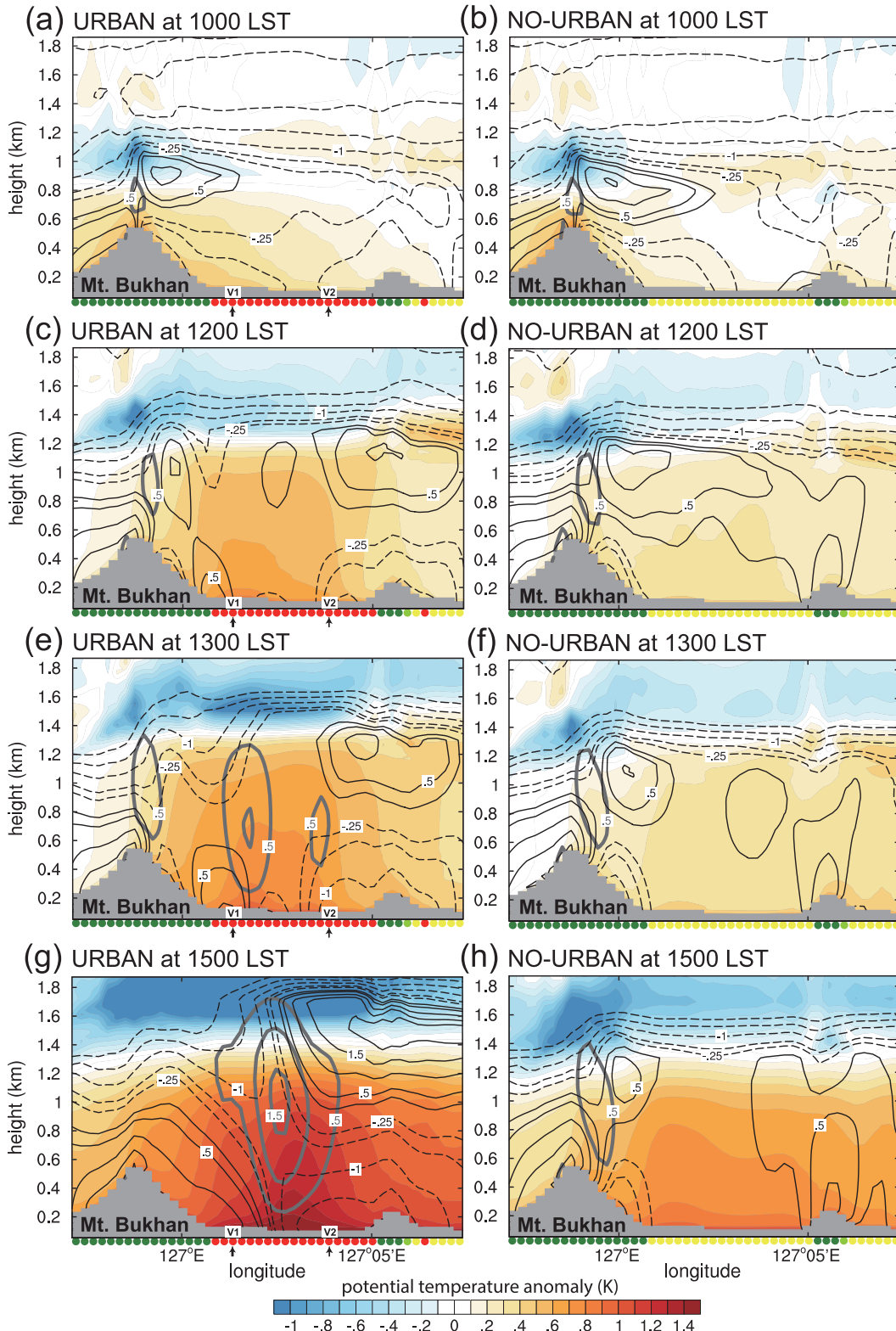


FIG. 5. Vertical cross sections of potential temperature anomaly (shaded), horizontal velocity in the east-west direction (thin solid and dashed lines), and vertical velocity (thick gray lines) along the line A-B in Fig. 8a (below) at (a) 1000, (c) 1200, (e) 1300, and (g) 1500 LST in the URBAN simulation and at (b) 1000, (d) 1200, (f) 1300, and (h) 1500 LST in the NO-URBAN simulation. The contour levels of horizontal velocity are $-2.0, -1.5, -1.0, -0.5, -0.25, 0.25, 0.5, 1.0, 1.5$, and 2.0 m s^{-1} . The contour levels of vertical velocity are $0.5, 1.0$, and 1.5 m s^{-1} . The dots on the x axis have the same colors as those used in Fig. 1c and indicate the LULC of each grid.

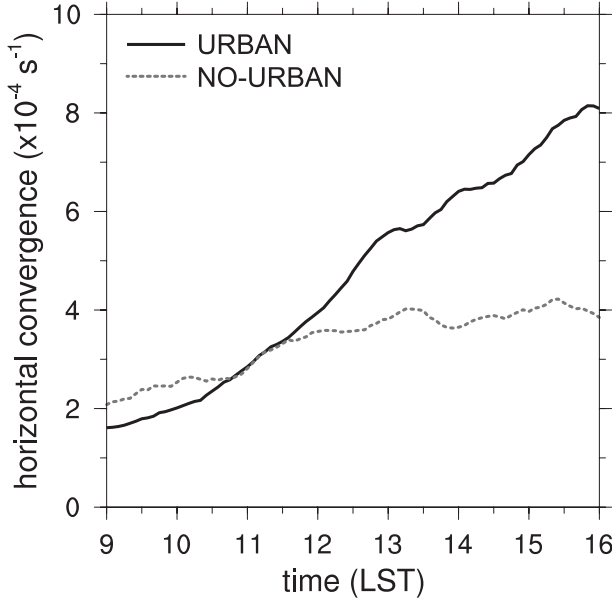


FIG. 6. Time variations of horizontal convergence averaged over the rectangular area marked in Fig. 8a (below) in the URBAN and NO-URBAN simulations. The wind field at the lowest fourth model level ($z \approx 250$ m) is used to calculate the convergence.

This mechanism is therefore responsible for the strong horizontal convergence in the late afternoon in the urbanized basin area (URBAN simulation) (Fig. 6).

c. River-breeze circulation and its interactions with other local circulations

On 24 June 2010, the river breeze starts to develop in the morning (see Figs. 4a,b) and increases in strength in the daytime. Figure 8 shows the horizontal and vertical velocity fields at $z = 600$ m in the URBAN simulation. In Figs. 8b–d, convergence zones with strong updrafts formed as a result of the interaction between the urban breeze and the river breeze are evident in the vicinity of the Han River, as mentioned in section 4a.

To examine the evolution of the river breeze and its interaction with the urban breeze, the vertical cross sections of potential temperature anomaly and wind along the line C–D (depicted in Fig. 8a) are presented in Fig. 9. At 1030 LST, in both simulations, the river-breeze circulation characterized by the divergent (convergent) flow in the lower (upper) boundary layer prevails near the Han River and the upslope wind develops along the slope of Mount Gwanak. Similar to the example examined in section 4b, the intensity of the upslope wind in the URBAN simulation is weaker owing to the UHI than that in the NO-URBAN simulation. In the NO-URBAN simulation, moreover, the upslope wind is combined with the divergent river breeze and hence its intensity is strong.

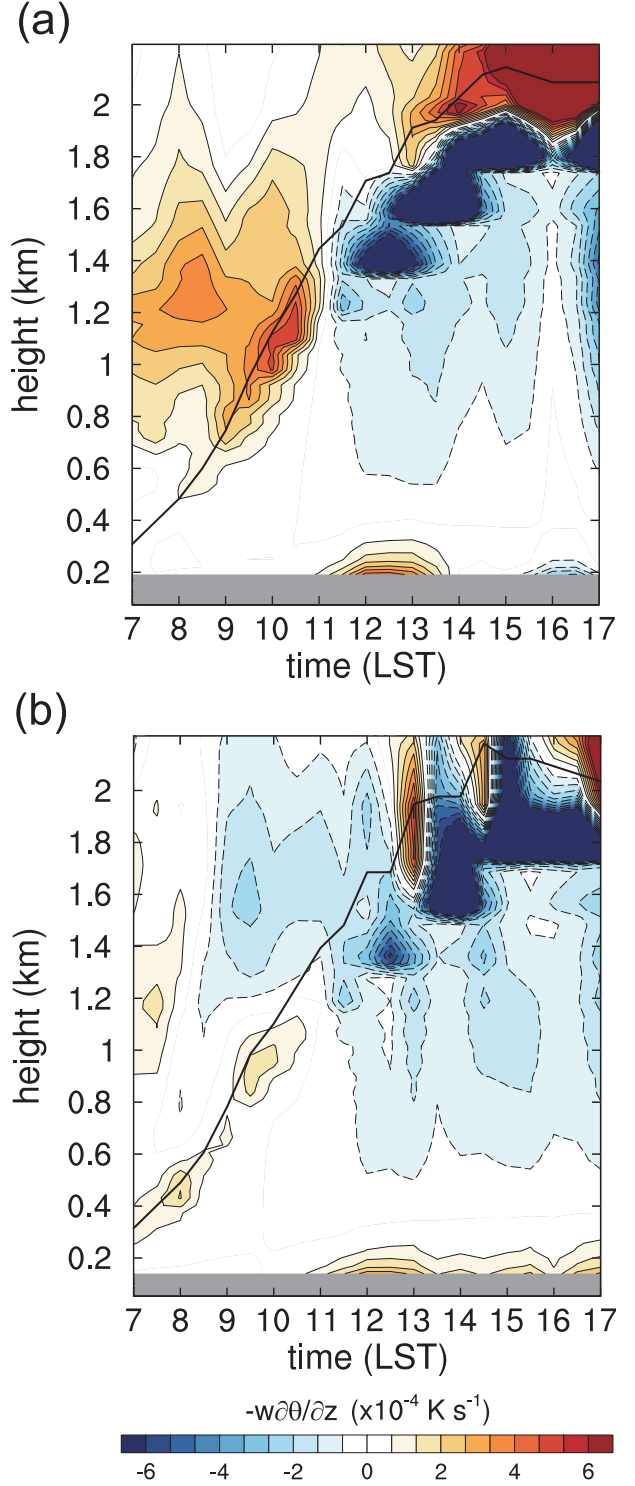


FIG. 7. Time–height fields of the term for the vertical advection of potential temperature ($-w\partial\theta/\partial z$) in the thermodynamic energy equation at points (a) V1 and (b) V2 in the URBAN simulation. Points V1 and V2 are indicated by the thick and thin arrows in Fig. 5, respectively. The thick line indicates the top of the boundary layer.

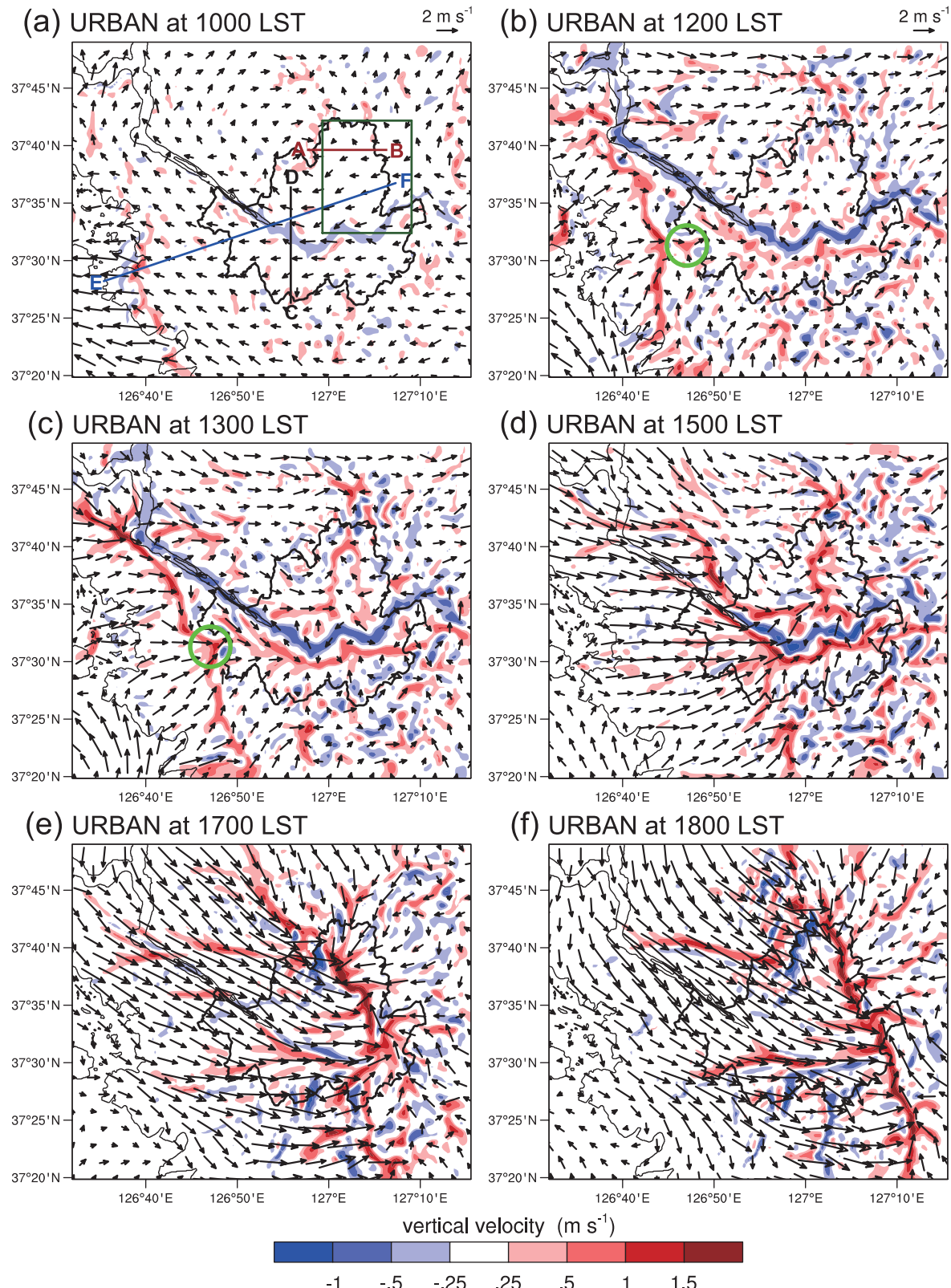


FIG. 8. Horizontal (vectors) and vertical velocity (colors) fields at $z = 600$ m at (a) 1000, (b) 1200, (c) 1300, (d) 1500, (e) 1700, and (f) 1800 LST in the URBAN simulation.

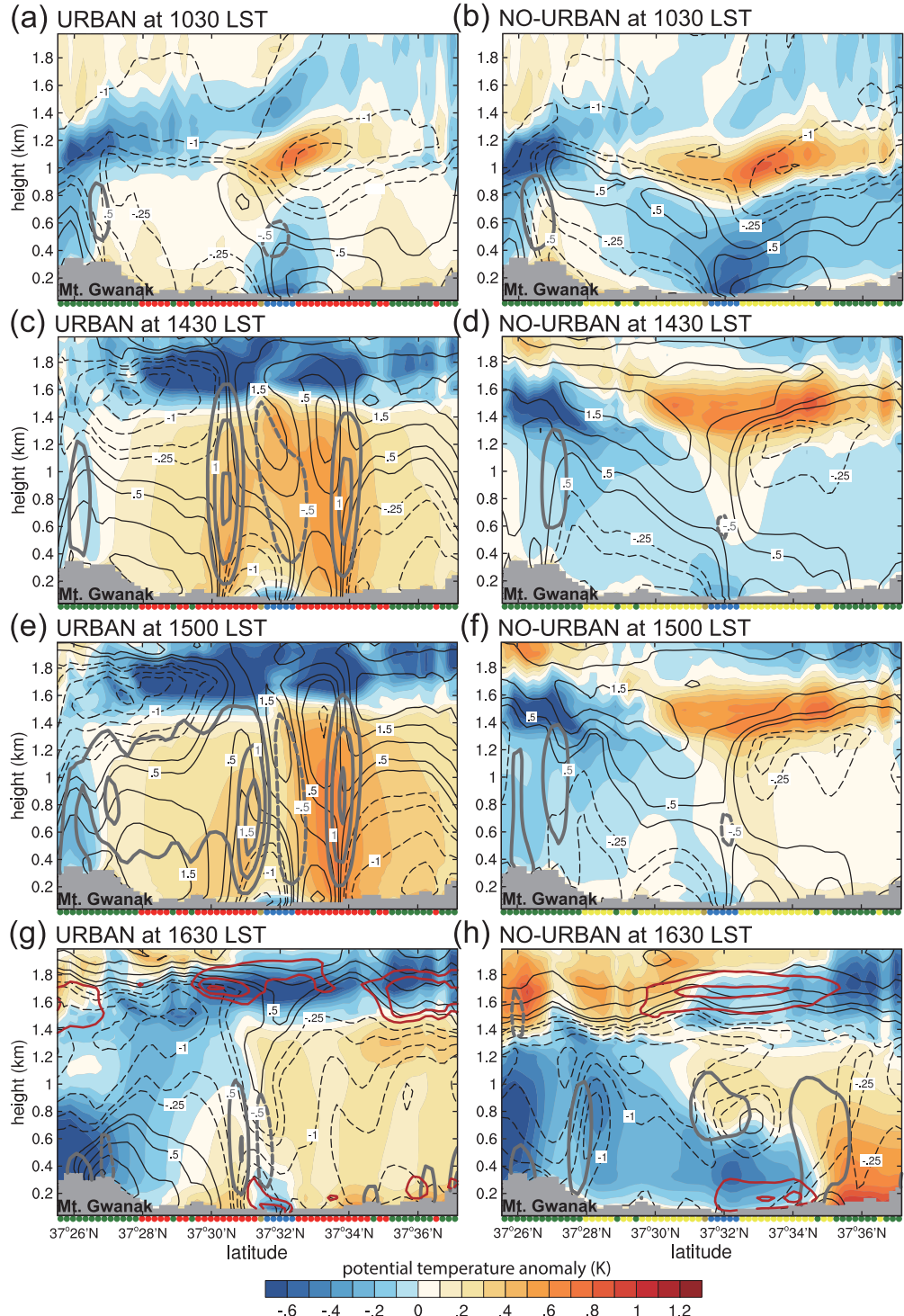


FIG. 9. Vertical cross sections of potential temperature anomaly (shaded), horizontal velocity in the north-south direction (thin solid and dashed black lines), vertical velocity (thick solid and dashed gray lines), and horizontal wind speed (thick red line) along the line C–D in Fig. 8a at (a) 1030, (c) 1430, (e) 1500, and (g) 1630 LST in the URBAN simulation and at (b) 1030, (d) 1430, (f) 1500, and (h) 1630 LST in the NO-URBAN simulation. The contour levels of horizontal velocity are $-2.0, -1.5, -1.0, -0.5, -0.25, 0.25, 0.5, 1.0, 1.5$, and 2.0 m s^{-1} . The contour levels of vertical velocity are $-0.5, 0.5, 1.0$, and 1.5 m s^{-1} . The contour levels of horizontal wind speed are $5.0, 5.5$, and 6.0 m s^{-1} . The dots on the x axis have the same colors as those used in Fig. 1c and indicate the LULC of each grid.

As the daytime UHI intensity increases in the afternoon (Fig. 3c), the upslope wind that develops along the slope of Mount Gwanak becomes indiscernible and a strong urban-breeze circulation develops in the southern and northern areas of Seoul (Fig. 9c). Meanwhile, the river-breeze circulation prevails in the vicinity of the Han River because of the much cooler river surface in comparison with the adjacent urban surface (e.g., $\sim 40^{\circ}\text{C}$ at 1500 LST), exhibiting divergent flow and downdrafts over the river. Furthermore, the large difference in air temperature between the river and the adjacent urban area induces a strong river breeze (Fig. 9c). Consequently, the two prevailing breezes form strong convergence zones in the southern and northern areas of Seoul adjacent to the river, producing strong upward motions there. In the NO-URBAN simulation, the combined circulation in the southern area of Seoul strengthens in the afternoon (Figs. 9d,f).

As the sea breeze penetrates inland, the sea-breeze front interacts with the updrafts that are formed as a result of the interaction between the urban breeze and the river breeze. For example, at 1500 LST (Figs. 8d and 9e), the vertical velocity at which the sea-breeze front encounters the updraft near the Han River is larger than at other locations. In Fig. 9e, the upward motion seen in the region from Mount Gwanak to the Han River represents the sea-breeze front. Thus, it can be said that the strong upward motion at the intersection point is a result of the interaction among the urban-breeze, river-breeze, and sea-breeze circulations.

A remarkable urban impact on the sea breeze that is found is an increase in the wind speed of the sea-breeze inflow along the river. Figure 9g shows that the wind speed of the sea-breeze inflow over the Han River is stronger than that over the adjacent land. This increase in wind speed along the river is also seen in the near-surface wind field in Fig. 4e (highlighted by gray arrows). The smaller roughness length of the river than that of the land is one of the possible reasons for the increase in wind speed along the river. Interestingly, the increase in wind speed is more prominent in the URBAN simulation than in the NO-URBAN simulation (cf. Fig. 9g with Fig. 9h). Because the marine air brought in by the sea-breeze inflow remains warm in the urban area, the difference in air temperature between the river and the adjacent urban area is large even after the intrusion of cool marine air (Figs. 4e and 9g). This leads to a large difference in boundary layer height between the river and the adjacent urban area (e.g., ~ 1500 m at 1630 LST). As the sea breeze blows over the river where the boundary layer is shallow, the wind speed of the sea-breeze inflow increases there. On the other hand, in the NO-URBAN simulation, the difference in air temperature between the

river and the adjacent cropland is small (Figs. 4f and 9h) and accordingly the difference in boundary layer height is small (e.g., ~ 400 m at 1630 LST). Thus, the increase in the wind speed of the sea-breeze inflow can be more prominent in the URBAN simulation.

d. Sea-breeze circulation and its interactions with other local circulations

Under the weak offshore-wind condition, the sea breeze develops with clearly detectable front (Fig. 8). In the daytime, the sea breeze in the URBAN and NO-URBAN simulations penetrates inland (Figs. 4 and 8). Figure 10 shows the location of the sea-breeze front following the line E–F (depicted in Fig. 8a) and the characteristics of the sea breeze in the URBAN and NO-URBAN simulations. The location of the sea-breeze front is determined as the position at which the gradient of horizontal wind speed in the horizontal direction within a lower region (~ 600 m deep) of the boundary layer and the vertical velocity are largest. In this study, the urban areas in the SMA are divided into three types: coastal urban area (C), inland urban area (I), and farther-inland urban area, namely Seoul urban area (S), for the sake of comprehensive understanding of urban impacts on the sea breeze (Fig. 1c).

At 1000 LST, the sea-breeze front in the two simulations has almost the same location (Fig. 10a). It is interesting that during 1030–1140 LST the sea breeze moves inland slightly faster in the NO-URBAN simulation than in the URBAN simulation (Fig. 10a) even though the air temperature ahead of the front is higher in the URBAN simulation (Fig. 10b). This is because the dynamical effect arising from the increased surface roughness of the coastal urban area plays a more important role in the inland penetration of the sea breeze than the thermal effect does during this period when the daytime UHI intensity is weak. The larger friction velocity behind the front in the URBAN simulation than in the NO-URBAN simulation explains the retardation of the inland penetration of the sea breeze (Fig. 10c). The friction velocity presented in Fig. 10c is the maximum value near the front within the marine air mass (u_{*SB}). This retardation due to the coastal urban area is consistent with the results of previous studies (e.g., Bornstein and Thompson 1981; Martilli 2003; Dandou et al. 2009; Chen et al. 2011). After passing through the coastal urban area, however, the sea breeze moves inland faster in the URBAN simulation than in the NO-URBAN simulation although u_{*SB} is consistently larger in the URBAN simulation. Thus, it is concluded that the dynamical effect has a dominant impact on the inland penetration of the sea breeze in its early development. Unlike the penetration speed of the sea breeze, in the morning, the maximum horizontal

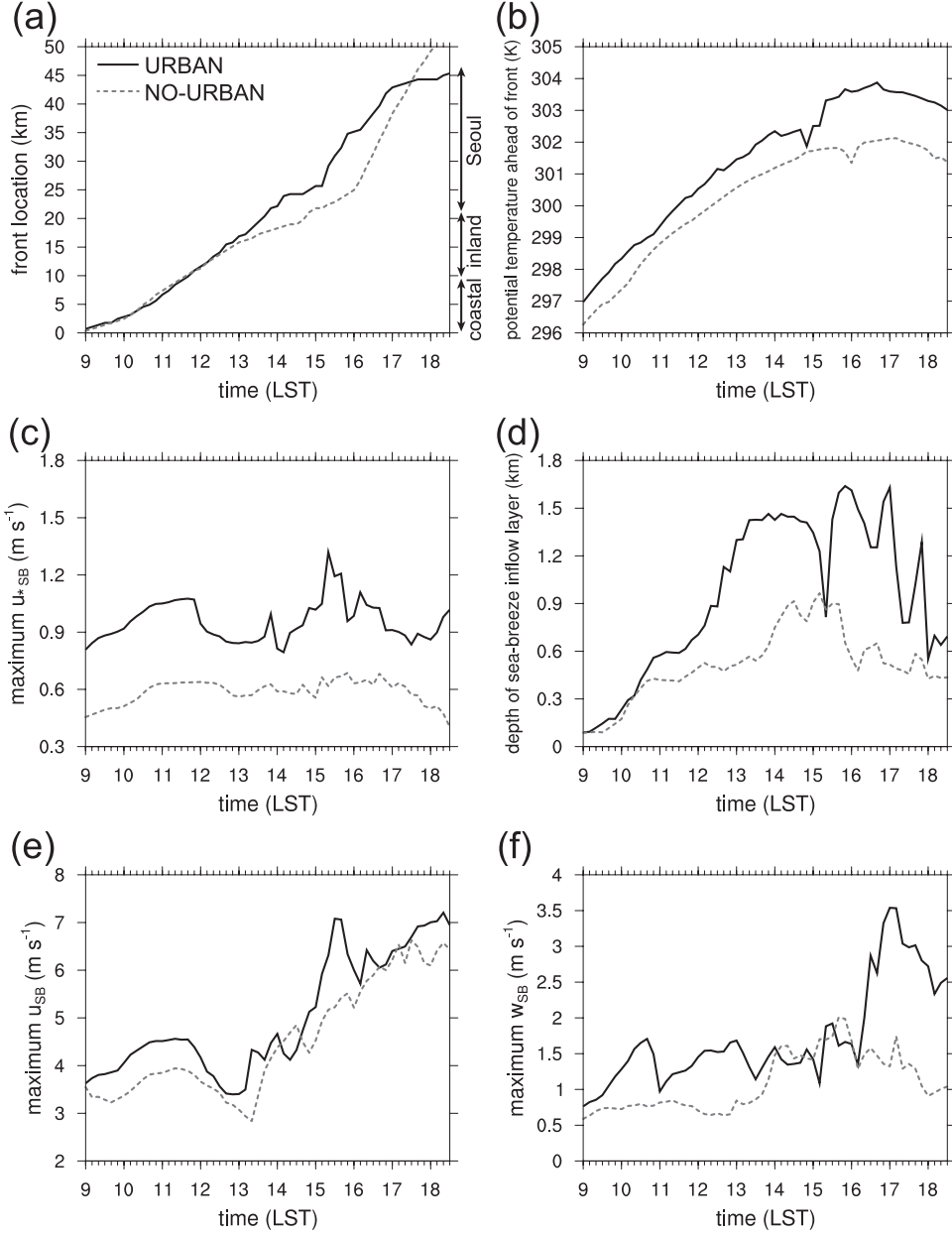


FIG. 10. (a) The location of sea-breeze front following the line E–F in Fig. 8a, (b) potential temperature ahead of the front at the lowest model level, (c) maximum friction velocity near the front within the marine air mass (u^*_{SB}), (d) depth of the sea-breeze inflow layer of the front, (e) maximum horizontal wind speed near the front within the marine air mass (u_{SB}), and (f) maximum vertical velocity of the front (w_{SB}) in the URBAN and NO-URBAN simulations.

wind speed near the front within the marine air mass (u_{SB}) and the maximum vertical velocity of the front (w_{SB}) are larger when the urban area is present than when the urban area is not present (Figs. 10e,f). In addition, the depth of the sea-breeze inflow layer (simply, depth of the inflow layer) is larger in the URBAN simulation (Fig. 10d). Here, the depth of the inflow layer is defined as the depth from the surface to the height where the

magnitude of the horizontal velocity in the east–west direction reaches its minimum, that is, roughly equal to the height of the upper boundary of the inflow layer. The stronger sea-breeze circulation and deeper inflow layer are due to the higher air temperature in the urban area. This is consistent with the results of previous studies (e.g., Yoshikado 1992; Fock and Schlünzen 2012).

Figure 11 shows the vertical cross sections of potential temperature, vertical velocity, and wind along the line E–F in the URBAN and NO-URBAN simulations. As shown in Fig. 10a, in the morning, the sea-breeze front moves inland slightly faster in the NO-URBAN simulation (Fig. 11b) than in the URBAN simulation (Fig. 11a). After passing through the coastal urban area, the location of the front in the URBAN simulation is almost the same as that in the NO-URBAN simulation (Figs. 11c,d). Over the inland urban area, it is seen that the air temperature ahead of the front is higher and accordingly the boundary layer is deeper in the URBAN simulation than in the NO-URBAN simulation. Additionally, the updraft that is seen in Fig. 11a over the inland urban area is intensified. This updraft is highlighted by the circle in Fig. 8b. The UHI in the inland urban area induces a relatively strong landward-convergent flow. This flow attracts the front toward the urban area, which is also seen in Fig. 8c (highlighted by the circle).

The updraft over the inland urban area merges with the sea-breeze front at 1300 LST, producing a strong upward motion (Fig. 11e). In addition, the depth of the inflow layer increases significantly (Fig. 10d). The increase in the depth of the inflow layer due to the interaction with the updraft is consistent with the observation in a non-urban environment by Laird et al. (1995). Yoshikado and Kondo (1989) observed a similar phenomenon wherein the mixing height over the suburban area of Tokyo, Japan, sharply increases from 0.6 to 1.7 km when the sea breeze reaches the suburban area. Yoshikado (1990) interpreted this as being attributed to the stagnant region formed over the suburban area.

A more noticeable urban impact on the sea breeze is that the inflow layer remains relatively deep over the inland urban area even after the sea-breeze front passes through the urban area (Fig. 11g). Even though the updraft over the urban area weakens with time because of the advection of cool marine air, the updraft still exists after the frontal passage. Consequently, the depth of the inflow layer shows an undulating feature along the path of the front. The uplift of the inflow layer over the updraft persists until late afternoon (not shown). The still prominent UHI in the marine air mass is responsible for the uplift of the inflow layer. On the other hand, no significant change in the depth of the inflow layer is seen in the NO-URBAN simulation (Figs. 11d,f,h). Thus, it is found that at the moment of the interaction between the updraft over the urban area and the sea-breeze front the sea-breeze circulation is intensified and the sea-breeze inflow layer is deepened, and that after the frontal passage the urban thermal effect is still exerted on the sea-breeze inflow layer.

As the sea breeze penetrates farther inland, the sea-breeze front merges with the strong updrafts that are

formed as a result of the interaction between the urban breeze and the river breeze and w_{SB} increases (Fig. 8d). When the front crosses the Han River, in contrast, w_{SB} decreases because of the consistently low air temperature over the river. Accordingly, the depth of the inflow layer abruptly decreases around 1520 LST (Fig. 10d). Zhong et al. (1991) showed a similar result that the magnitude of upward motion of a sea-breeze front is reduced by a factor of 5 as the front crosses the Indian River, Florida. In addition, the divergent river breeze acts to inhibit penetration of the sea breeze farther inland prior to crossing the river. Therefore, the sea-breeze front tends to stagnate near the river during 1410–1510 LST in the URBAN simulation and moves inland at a slow rate during 1500–1600 LST in the NO-URBAN simulation (Fig. 10a). Note that the time at which the sea-breeze front crosses the Han River is different in the two simulations. As highlighted in section 4c, u_{SB} increases considerably over the Han River when the urban area is present, that is, at around 1530 LST in the URBAN simulation (Fig. 10e). The u_{SB} in the NO-URBAN simulation, however, does not show a significant change when the sea-breeze front crosses the river.

After crossing the Han River, the sea-breeze front enters the northern area of Seoul and then the sea breeze interacts strongly with the urban breeze that develops there (e.g., Figs. 8e,f). For example, in Fig. 8e, the strong upward motion resulting from the interaction between the urban breeze and the sea breeze is seen, with a maximum vertical velocity of 2.9 m s^{-1} . The air temperature in the mid/late afternoon in the northern area of Seoul is high, and hence the inland penetration of the sea breeze in the URBAN simulation is accelerated after crossing the Han River (Figs. 10a,b). This acceleration of the front is consistent with the results of previous studies (e.g., Khan and Simpson 2001; Freitas et al. 2007). Similar to the example shown in Fig. 11, the abrupt increases in the depth of the inflow layer at around 1550, 1700, and 1750 LST in the URBAN simulation correspond to the interactions between the updrafts over Seoul and the sea-breeze front.

Because the inward flow toward the center of Seoul that forms part of the urban breeze acts to inhibit penetration of the sea breeze farther inland, the sea breeze stalls near the eastern boundary of Seoul (Fig. 8f). The decrease in the penetration speed of the sea breeze in the late afternoon/early evening is clearly evident in the URBAN simulation as compared with the NO-URBAN simulation (Fig. 10a). The sea-breeze front in the URBAN simulation stagnates in Seoul during 1700–1830 LST. This stagnation due to the inland urban area (Seoul urban area) is consistent with the results of previous studies (e.g., Freitas et al. 2007). It is noteworthy that not only the

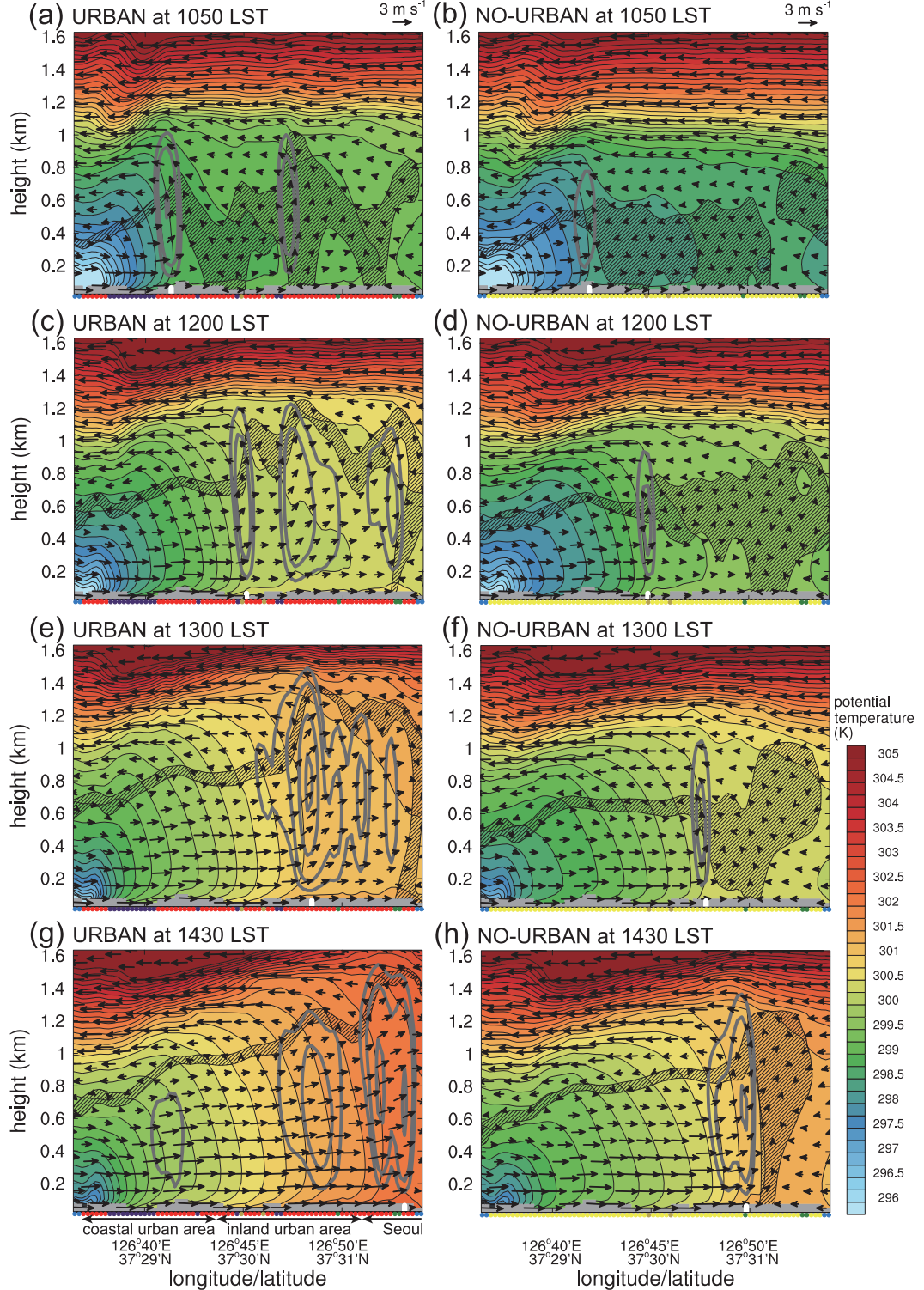


FIG. 11. Vertical cross sections of potential temperature (shaded with thin lines), vertical velocity (thick gray lines), and wind (vectors) along the line E–F at (a) 1050, (c) 1200, (e) 1300, and (g) 1430 LST in the URBAN simulation and at (b) 1050, (d) 1200, (f) 1300, and (h) 1430 LST in the NO-URBAN simulation. The contour levels of vertical velocity are 0.3, 0.5, 1.0, and 1.5 m s^{-1} . The hatched area is where the horizontal velocity in the east–west direction ranges from 0.0 to 0.25 m s^{-1} in magnitude. The location of sea-breeze front is indicated by the thick, short white bar on the x axis. The dots on the x axis have the same colors as those used in Fig. 1c and indicate the LULC of each grid.

thermal effect due to the urban surface but also the thermal effect due to topography contributes to the stagnation of the sea breeze. In section 4b, it is shown that the high air temperature in the urban valley resulting from the combined effect induces the strong plain-side urban breeze in the late afternoon. The stronger inward flow opposing the inland penetration of the sea breeze leads to the stagnation of the sea breeze in the urbanized basin area.

5. Summary and conclusions

Daytime local circulations, such as urban-breeze, cross-valley, river-breeze, and sea-breeze circulations, and their interactions under a weak synoptic-wind condition were investigated using the WRF-SNUUCM coupled model. In the morning, the cross-valley circulation is predominant in the valley region. As the daytime UHI intensity increases in the afternoon and accordingly the urban-breeze circulation increases in strength, the urban-breeze circulation dominates over the cross-valley circulation in the valley region. While the mountainside urban-breeze circulation weakens because of the cross-valley circulation in the opposite direction, the plain-side urban-breeze circulation away from the mountain strengthens because of the combined effect of heating from the urban surface and subsidence heating associated with the cross-valley circulation. In addition, the strengthened urban breeze due to the combined effect acts to inhibit penetration of the sea breeze farther inland. Consequently, the sea breeze stagnates in Seoul.

The river breeze develops near the Han River in response to the differential surface heating between the river and land. Because of the larger difference in air temperature between the river and the adjacent urban area, the intensity of the river breeze is stronger when the urban area is present (URBAN simulation) than when it is absent (NO-URBAN simulation). As a result of the interaction between the urban breeze and the river breeze, convergence zones with strong updrafts are formed in the vicinity of the river. When the sea-breeze front interacts with the updrafts in the convergence zones, the vertical velocity of the front at the intersection points increases considerably. When the sea-breeze front crosses the Han River, the cool air over the river causes the vertical velocity of the front and the depth of the sea-breeze inflow layer to decrease. Interestingly, the wind speed of the sea-breeze inflow over the river increases. This increase in wind speed along the river is considerable when the urban area is present because of the large difference in air temperature and the corresponding large difference in boundary layer height between the river and the adjacent urban area.

It was found that the presence of the urban area modifies the sea-breeze circulation and its penetration speed. In the morning, when the sea breeze moves over the coastal urban area, the inland penetration of the sea breeze is retarded because of the increased surface roughness of the coastal urban area. After passing through the coastal urban area, the sea breeze moves inland faster in the URBAN simulation than in the NO-URBAN simulation owing to the landward-convergent flows induced by the UHIs in the inland urban areas. As the sea-breeze front interacts with the updrafts formed over the inland urban areas, the vertical velocity of the front and the depth of the inflow layer at the intersection points increase significantly. Even after the frontal passage, the urban thermal effect still contributes to warming and deepening the sea-breeze inflow layer.

In this study, a fair-weather condition is considered. The degree of interactions among the local circulations would differ under different weather conditions. Further research under different weather conditions would be required.

Acknowledgments. The authors are grateful to two anonymous reviewers for providing valuable comments on this work. This work was supported by the National Research Foundation of Korea (NRF) grant funded by the Korea Ministry of Education, Science and Technology (MEST) (2012-0005674).

REFERENCES

- Bornstein, R. D., and W. T. Thompson, 1981: Effects of frictionally retarded sea breeze and synoptic frontal passages on sulfur dioxide concentrations in New York City. *J. Appl. Meteor.*, **20**, 843–858.
- , E. Gutiérrez, J. E. González, A. Martilli, F. Chen, and J. Ching, 2012: Horizontal-vortices in WRF simulations of NYC: Real or not? *Proc. Eighth Int. Conf. on Urban Climate*, Dublin, Ireland, International Association for Urban Climate, PM3E/672.
- Chen, F., and J. Dudhia, 2001: Coupling an advanced land surface-hydrology model with the Penn State–NCAR MM5 modeling system. Part I: Model implementation and sensitivity. *Mon. Wea. Rev.*, **129**, 569–585.
- , S. Miao, M. Tewari, J.-W. Bao, and H. Kusaka, 2011: A numerical study of interactions between surface forcing and sea breeze circulations and their effects on stagnation in the greater Houston area. *J. Geophys. Res.*, **116**, D12105, doi:10.1029/2010JD015533.
- Crosman, E. T., and J. D. Horel, 2010: Sea and lake breezes: A review of numerical studies. *Bound.-Layer Meteor.*, **137**, 1–29.
- Dandou, A., M. Tombrou, and N. Soulakellis, 2009: The influence of the city of Athens on the evolution of the sea-breeze front. *Bound.-Layer Meteor.*, **131**, 35–51.
- Dirks, R. A., 1974: Urban atmosphere: Warm dry envelope over St. Louis. *J. Geophys. Res.*, **79**, 3473–3475.

- Dudhia, J., 1989: Numerical study of convection observed during the Winter Monsoon Experiment using a mesoscale two-dimensional model. *J. Atmos. Sci.*, **46**, 3077–3107.
- Farr, T. G., and Coauthors, 2007: The shuttle radar topography mission. *Rev. Geophys.*, **45**, RG2004, doi:10.1029/2005RG000183.
- Fock, B. H., and K. H. Schlünzen, 2012: Characterization of typical coastal circulations with high-resolution measurements in the Gulf of Valencia. *Int. J. Climatol.*, **32**, 1392–1405.
- Freitas, E. D., C. M. Rozoff, W. R. Cotton, and P. L. Silva Dias, 2007: Interactions of an urban heat island and sea-breeze circulations during winter over the metropolitan area of São Paulo, Brazil. *Bound.-Layer Meteor.*, **122**, 43–65.
- Giridharan, R., S. S. Y. Lau, S. Ganesan, and B. Givoni, 2007: Urban design factors influencing heat island intensity in high-rise high-density environments of Hong Kong. *Build. Environ.*, **42**, 3669–3684.
- Hidalgo, J., V. Masson, and G. Pigeon, 2008a: Urban-breeze circulation during the CAPITOUL experiment: Numerical simulations. *Meteor. Atmos. Phys.*, **102**, 243–262.
- , G. Pigeon, and V. Masson, 2008b: Urban-breeze circulation during the CAPITOUL experiment: Observational data analysis approach. *Meteor. Atmos. Phys.*, **102**, 223–241.
- Hong, S.-Y., and J.-O. J. Lim, 2006: The WRF single-moment 6-class microphysics scheme (WSM6). *J. Korean Meteor. Soc.*, **42**, 129–151.
- , Y. Noh, and J. Dudhia, 2006: A new vertical diffusion package with an explicit treatment of entrainment processes. *Mon. Wea. Rev.*, **134**, 2318–2341.
- Kain, J. S., 2004: The Kain–Fritsch convective parameterization: An update. *J. Appl. Meteor.*, **43**, 170–181.
- Khan, S. M., and R. W. Simpson, 2001: Effect of a heat island on the meteorology of a complex urban airshed. *Bound.-Layer Meteor.*, **100**, 487–506.
- Kim, Y.-H., and J.-J. Baik, 2002: Maximum urban heat island intensity in Seoul. *J. Appl. Meteor.*, **41**, 651–659.
- Knilevel, J. C., G. H. Bryan, and J. P. Hacker, 2007: Explicit numerical diffusion in the WRF model. *Mon. Wea. Rev.*, **135**, 3808–3824.
- Laird, N. F., D. A. R. Kristovich, R. M. Rauber, H. T. Ochs III, and L. J. Miller, 1995: The Cape Canaveral sea and river breezes: Kinematic structure and convective initiation. *Mon. Wea. Rev.*, **123**, 2942–2956.
- Lee, S.-H., and F. Kimura, 2001: Comparative studies in the local circulations induced by land-use and by topography. *Bound.-Layer Meteor.*, **101**, 157–182.
- Lee, S.-H., C.-K. Song, J.-J. Baik, and S.-U. Park, 2009: Estimation of anthropogenic heat emission in the Gyeong-In region of Korea. *Theor. Appl. Climatol.*, **96**, 291–303.
- Lemonsu, A., and V. Masson, 2002: Simulation of a summer urban breeze over Paris. *Bound.-Layer Meteor.*, **104**, 463–490.
- Martilli, A., 2003: A two-dimensional numerical study of the impact of a city on atmospheric circulation and pollutant dispersion in a coastal environment. *Bound.-Layer Meteor.*, **108**, 91–119.
- Mlawer, E. J., S. J. Taubman, P. D. Brown, M. J. Iacono, and S. A. Clough, 1997: Radiative transfer for inhomogeneous atmospheres: RRTM, a validated correlated- k model for the longwave. *J. Geophys. Res.*, **102**, 16 663–16 682.
- Ohashi, Y., and H. Kida, 2002: Effects of mountains and urban areas on daytime local-circulations in the Osaka and Kyoto regions. *J. Meteor. Soc. Japan*, **80**, 539–560.
- Rampanelli, G., D. Zardi, and R. Rotunno, 2004: Mechanisms of up-valley winds. *J. Atmos. Sci.*, **61**, 3097–3111.
- Ries, H., and K. H. Schlünzen, 2009: Evaluation of a mesoscale model with different surface parameterizations and vertical resolutions for the Bay of Valencia. *Mon. Wea. Rev.*, **137**, 2646–2661.
- Ryu, Y.-H., J.-J. Baik, and S.-H. Lee, 2011: A new single-layer urban canopy model for use in mesoscale atmospheric models. *J. Appl. Meteor. Climatol.*, **50**, 1773–1794.
- Shin, H. H., and S.-Y. Hong, 2011: Intercomparison of planetary boundary-layer parametrizations in the WRF model for a single day from CASES-99. *Bound.-Layer Meteor.*, **139**, 261–281.
- Shreffler, J. H., 1978: Detection of centripetal heat-island circulations from tower data in St. Louis. *Bound.-Layer Meteor.*, **15**, 229–242.
- Skamarock, W. C., and Coauthors, 2008: A description of the Advanced Research WRF Version 3. NCAR Tech. Note NCAR/TN-475+STR, 113 pp.
- Thompson, W. T., T. Holt, and J. Pullen, 2007: Investigation of a sea breeze front in an urban environment. *Quart. J. Roy. Meteor. Soc.*, **133**, 579–594.
- Wong, K. K., and R. A. Dirks, 1978: Mesoscale perturbations on airflow in the urban mixing layer. *J. Appl. Meteor.*, **17**, 677–688.
- Yoshikado, H., 1990: Vertical structure of the sea breeze penetrating through a large urban complex. *J. Appl. Meteor.*, **29**, 878–891.
- , 1992: Numerical study of the daytime urban effect and its interaction with the sea breeze. *J. Appl. Meteor.*, **31**, 1146–1164.
- , 1994: Interaction of the sea breeze with urban heat islands of different sizes and locations. *J. Meteor. Soc. Japan*, **72**, 139–143.
- , and H. Kondo, 1989: Inland penetration of the sea breeze over the suburban area of Tokyo. *Bound.-Layer Meteor.*, **48**, 389–407.
- Zhong, S., J. M. Leone Jr., and E. S. Takle, 1991: Interaction of the sea breeze with a river breeze in an area of complex coastal heating. *Bound.-Layer Meteor.*, **56**, 101–139.